

# The diurnal path to persistent convective self-aggregation

Gorm Gruner Jensen<sup>1</sup>, Romain Fiévet<sup>1</sup>, and Jan O. Haerter<sup>1,2,3</sup>

<sup>1</sup>Niels Bohr Institute, Copenhagen University, Blegdamsvej 17, 2100 Copenhagen, Denmark

<sup>2</sup>Complexity and Climate, Leibniz Center for Tropical Marine Research, Fahrenheitstrasse 6, 28359 Bremen, Germany

<sup>3</sup>Jacobs University Bremen, Campus Ring 1, 28759 Bremen, Germany

August 24, 2021

**Clustering of tropical thunderstorms constitutes an important climate feedback because it influences the heat radiated to space. Convective self-aggregation (CSA) is a profound modelling paradigm for explaining the clustering of tropical oceanic thunderstorms. However, CSA is hampered in the realistic limit of fine model resolution when cold pools—dense air masses beneath thunderstorm clouds—are well-resolved. Studies on CSA usually assume the surface temperature to be constant, despite realistic surface temperatures varying significantly between night and day, even over the sea. Here we mimic oscillating surface temperatures in cloud resolving numerical experiments and show that, in the presence of a diurnal cycle, CSA is enabled by high resolutions. We attribute this finding to vigorous combined cold pools emerging in symbiosis with mesoscale convective systems. Such cold pools suppress buoyancy in extended regions (~100 km) and enable the formation of persistent dry patches. Our findings help clarify how the tropical cloud field forms sustained clusters under realistic conditions and may have implications for the origin of extreme thunderstorm rainfall and tropical cyclones.**

CSA refers to the spatial separation into deep convective and dry subregions occurring spontaneously in numerical simulations with homogeneous boundary and initial conditions<sup>1–4</sup>. CSA serves as a plausible mechanism for observed large-scale tropical convective clustering, including the Madden-Julian oscillation<sup>5</sup> or the formation of tropical cyclones.<sup>6</sup> Modelling suggests that CSA typically hinges on local radiation feedbacks<sup>7–11</sup>. Maintenance of CSA has been attributed to a large-scale circulation resulting in an upgradient moisture transport<sup>8,9,12,13</sup>. The circulation is driven by a combination of moist adiabatic lifting in the convectively active region and enhanced radiative cooling in the dry region which must be compensated by subsidence heating. The initial harbinger of CSA is the formation of several small persistent dry patches<sup>4</sup>. At this initial stage, low cloud<sup>7</sup> and moisture feedbacks<sup>8,9</sup> within dry regions were found to be critical for overcoming the re-distribution of moisture by negative feedbacks<sup>3</sup>. Cold pools (CPs)—

density currents produced by rain re-evaporation beneath thunderstorm clouds—were reported to act against such clustering<sup>9,14–16</sup>. Also finer horizontal grid resolution, which intensifies CP effects<sup>7,17,18</sup>, hampered the onset.

Whereas CSA studies often specialise to temporally constant boundary conditions<sup>4</sup>, it is observationally evident that also temporal variations influence the spatial characteristics of convective rainfall<sup>19–25</sup>. Indeed, over continents, where surface temperatures oscillate strongly between day and night, a large fraction of extreme rainfall results from mesoscale convective systems (MCSs)<sup>26,27</sup>. MCS are defined as thunderstorm clusters exceeding 100 kilometres spatially and three hours temporally<sup>28</sup>. Despite indications that MCS rainfall rates and volumes might be increasing<sup>29,30</sup>, the forecast performance for MCS remains low<sup>31,32</sup>.

Several studies mimic diurnal variation through oscillating surface temperatures<sup>33–37</sup>. Under such conditions, recent simulations demonstrated spontaneous formation of MCS-like clusters<sup>38</sup>, which appeared only when the surface temperature amplitude was sufficiently large ( $\gtrsim 3.5 K$ ). The clusters were attributed to vigorous “combined cold pools,” which were able to force moist boundary layer air to the level of free convection. When the amplitude was smaller ( $\lesssim 2 K$ ), neither MCSs nor combined cold pools were detected and the organisational pattern was similar to the near-random pattern during early stages of radiative-convective equilibrium (RCE) simulations. The organisational pattern observed in the presence of a large diurnal amplitude—referred to as “diurnal self-aggregation” (DSA)—is similar to CSA in that clustering occurs spontaneously and is concentrated in parts of the spatial domain. However, DSA differs from CSA as clusters organise into patterns that are anti-correlated from day to day, such that an area receiving pronounced rain on a given day will typically receive weak rain, or none at all, on the following.

Here, we use a simulation setup that yields classical CSA under constant boundary conditions, when resolution is coarse, but fails to yield CSA when resolution is fine. We find that for time-varying boundary conditions the alternating

arXiv:2104.01132v1 [physics.ao-ph] 2 Apr 2021

day-to-day dynamics is accompanied by a persistent pattern of dry and rain-free patches. The locked-in patches closely resemble those at the onset of classical CSA. Contrary to CSA, these dry patches preferably occur at high numerical resolutions. Thus, our results introduce an organisational mechanism that is relevant in the realistic limit of high spatial model resolution and we draw a connection between the origin of continental extreme events, caused by MCS, and that of persistent cloud clumping over the tropical ocean.

**Numerical experiments:** We study cloud resolving numerical experiments using horizontally square domains of linear size  $L$  with laterally periodic boundary conditions at horizontal resolutions  $dx$  of .5, 1, 2 and 4 kilometres. Domain size is chosen as  $L = 480$  km for  $dx = .5$  km and  $L = 960$  km otherwise (Tab. 1). In our diurnal cycle experiments — termed DIU — we prescribe a spatially uniform, but temporally harmonic surface temperature,  $T_s(t)$ , defined by a one day period and a  $\pm 5$  K amplitude, such that  $T_s(t)$  oscillates around the average temperature  $\bar{T}_s \equiv 298$  K. To mimic a forested land surface, we reduce surface latent heat fluxes to 70 percent of the value for a sea surface. Insolation peaks at noon and vanishes at night, but plays a minor role due to the prescribed surface temperature. Each experiment is paired by a control experiment — termed RCE — where all settings are preserved except that surface temperature and insolation are both kept constant at the respective time averages (*Details: Methods*).

## Two layers of convective organization

Consider DIU and RCE at 1 km resolution, termed DIU-1km and RCE-1km, respectively (Fig. 1). After a short spin-up period, rain intensity remains nearly constant in RCE-1km. In DIU-1km, the oscillating  $T_s(t)$  is reflected in oscillations in domain mean rain intensity, with a pronounced afternoon peak and mostly rain-free nocturnal conditions (Fig. 1a). Daily-mean rainfall is, however, very similar in the two experiments.

Whereas RCE-1km shows no sign of CSA (Fig 1e), the spatial pattern emerging in DIU-1km is strikingly different: during the first few days the rainfall develops a patchy mesoscale pattern with rain clusters measuring on the order of one hundred kilometres across (Fig. 1b, 5th and 6th day), in compliance with previous findings<sup>38</sup>. However, ten days later (days 15 and 16), the dynamics follows a more complex pattern: in addition to the now larger and more intense MCSs the domain is also spotted with persistently rain-free patches. This persistent lack of rainfall becomes particularly clear, when considering rainfall averaged during multiple days (Fig 1f).

To generate the patterning found in DIU-1km, two separate mechanisms appear to be active: (i) a negative feedback inhibiting convective activity in areas where rain was particularly abundant the day before; (ii) a positive feedback which can preserve inactivity from day to day. To analyse these feedbacks further, we turn to the horizontal moisture field  $q_t(z, t)$  at each vertical model level  $z$  and

describe its temporal evolution from day to day using the 24h-lag correlation  $C_{24h}(q_t; t, z)$  (*Details: Methods*). Early morning is chosen as a reference, because at this time the moisture field is diffusively smoothed due to the absence of convective activity. Examining the vertical profile of  $C_{24h}(q_t; t, z)$  reveals an interesting dynamical structure of two pronounced extrema (Fig. 1g): a global minimum near 1.2 km and a global maximum near 3.5 km, indicative of alternating moisture patterns at the lower, but persistent moisture patterns at the upper level. In the course of the simulation, the correlations generally increase towards more positive values and by day 14 even the minimum at 1.2 km appears to switch to positive values.

The moisture pattern at this lower level, which corresponds approximately to cloud base, closely mirrors that of the rainfall (*compare* Fig. 1b and d). Examples are highlighted by black squares: at 4d4h, there is a strong positive moisture anomaly at  $z=1.2$  km. On the following (fifth) day that region receives intense rainfall, resulting in an intense drying near the cloud base (at 5d5h). On the sixth day, the area receives almost no rainfall.

The positive 24h-lag correlation in the free troposphere ( $z = 3.5$  km) implies persistence from day to day. Indeed, inspecting an example of a persistently dry patch (circled in Fig. 1b,c,d), rainfall is absent in the same region during consecutive days. Rather than replenishing the moisture within the persistently dry patches, rain clusters now appear to transport moisture elsewhere, undergoing a day-to-day oscillatory dynamics that specifically avoids the dry patches. Hence, despite the initial day-to-day alternation in rainfall pattern, later days show sustained rain-free sub-regions — suggesting that a form of CSA might eventually emerge in DIU-1km. The persistent dry patches described here emerge even faster for in DIU-500m (Fig. S1 vs. Fig. 1).

## Stronger clustering at higher resolutions

To quantify spatial rainfall variability at scales beyond that of individual raincells, we compute the relative standard deviation (RSD) of a coarse-grained rainfall field  $\bar{R}$ , where rainfall is block-averaged over  $32 \text{ km} \times 32 \text{ km}$  horizontally and 48 hours temporally (*Details: Methods*). The coarse-graining discounts small-scale fluctuations due to individual raincells and their cold pools, as well as any day-to-day alternation. The 32 km spatial scale is practically relevant as it corresponds the size of large metropolitan areas.

RCE-4km shows a clear trend of increasing  $\text{RSD}(\bar{R})$ , a typical feature of classical CSA<sup>3,4</sup>. However, for horizontal resolutions of 2 km or finer, the RCE experiments show no sign of CSA (Fig. 2a,b) and  $\text{RSD}(\bar{R})$  remains constant over time. This result agrees with the existing literature, which generally states that in RCE simulations CSA is inhibited by fine resolutions<sup>4,9</sup>.

In DIU, however, persistent rain-free patches are visible at 1 km resolution resulting in  $\text{RSD}(\bar{R})$  rapidly increases over time. The increase is even more pronounced in DIU-500m, despite the smaller domain size which is also often

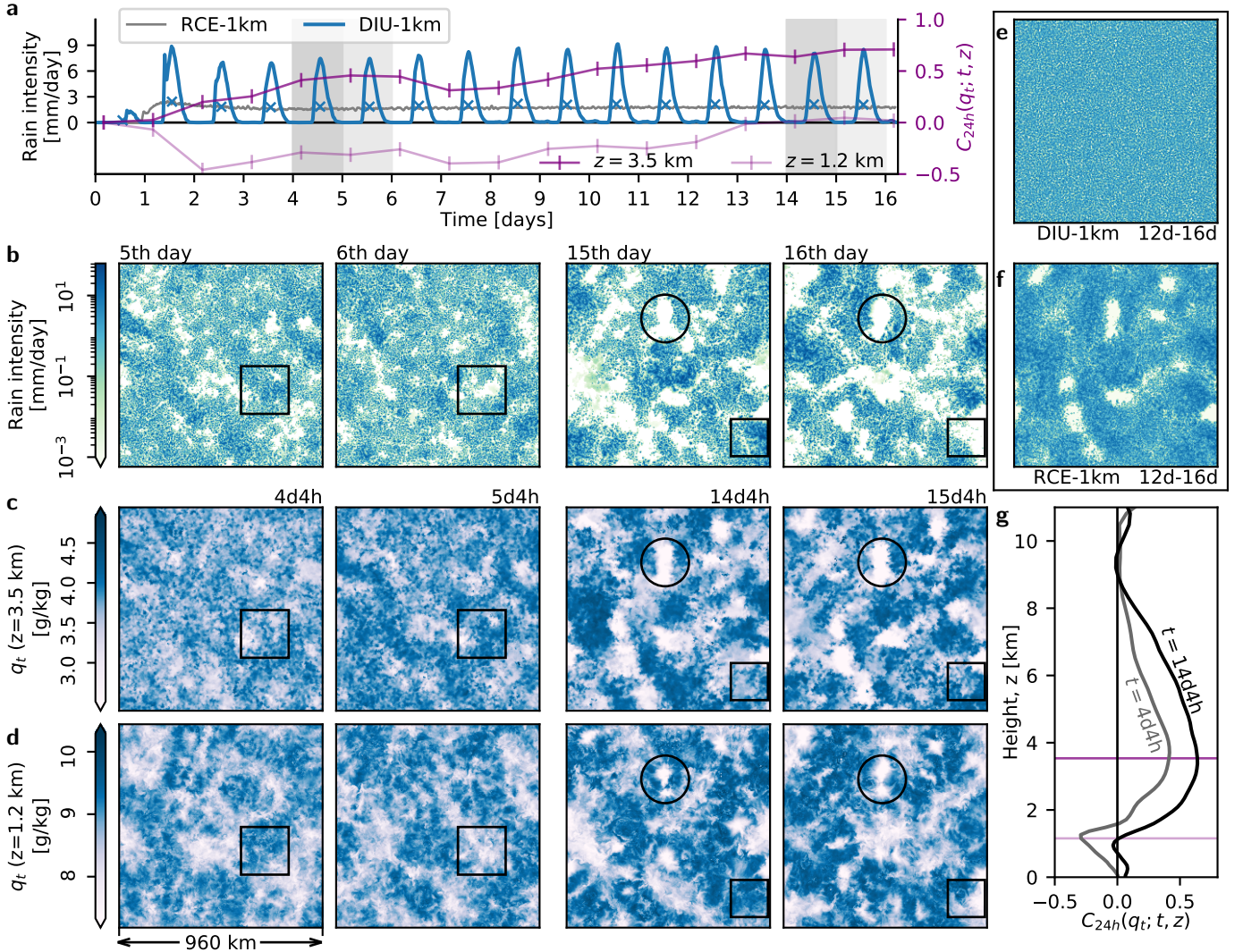


Figure 1: **Spatio-temporal organisation by diurnal surface temperature oscillations.** **a**, Time series of domain-mean rain intensity in RCE-1km (grey curve) and DIU-1km (blue curve). Blue  $\times$ -symbols indicate daily-average rain intensity in DIU-1km. Dark and faint purple curves show time series of 24-hour Pearson correlations,  $C_{24h}(q_t; t, z)$  for total water mixing ratio,  $q_t$ , for  $z = 3.5$  km and  $z = 1.2$  km respectively, with  $t$  taken at 4h on any given day (*Details: Methods*). **b**, Daily surface rainfall intensity, temporally-averaged over the 5th, 6th, 15th and 16th day. Corresponding averaging periods indicated by grey shades in (a). **c**, Early-morning (4h) horizontal field of  $q_t(t, x, y, z)$  for  $z = 3.5$  km at times corresponding to the days in (b). **d**, Analogous to (c) but for  $z = 1.2$  km. Black squares and circles in (b)–(d) highlight regions discussed in the main text. **e**, Four-day average rain intensity from day 13–16 in RCE-1km. The colour scale is the same as for panel (b). Note the lack of spatial organisation. **f**, Analogous to (e), but for DIU-1km. Note the rain-free patches. **g**,  $C_{24h}(q_t; t, z)$  vertical profiles, with  $t = 4d4h$  (grey) and  $t = 14d4h$  (black), respectively. The horizontal dark and faint purple lines indicate the respective vertical levels used in (a), (c) and (d).

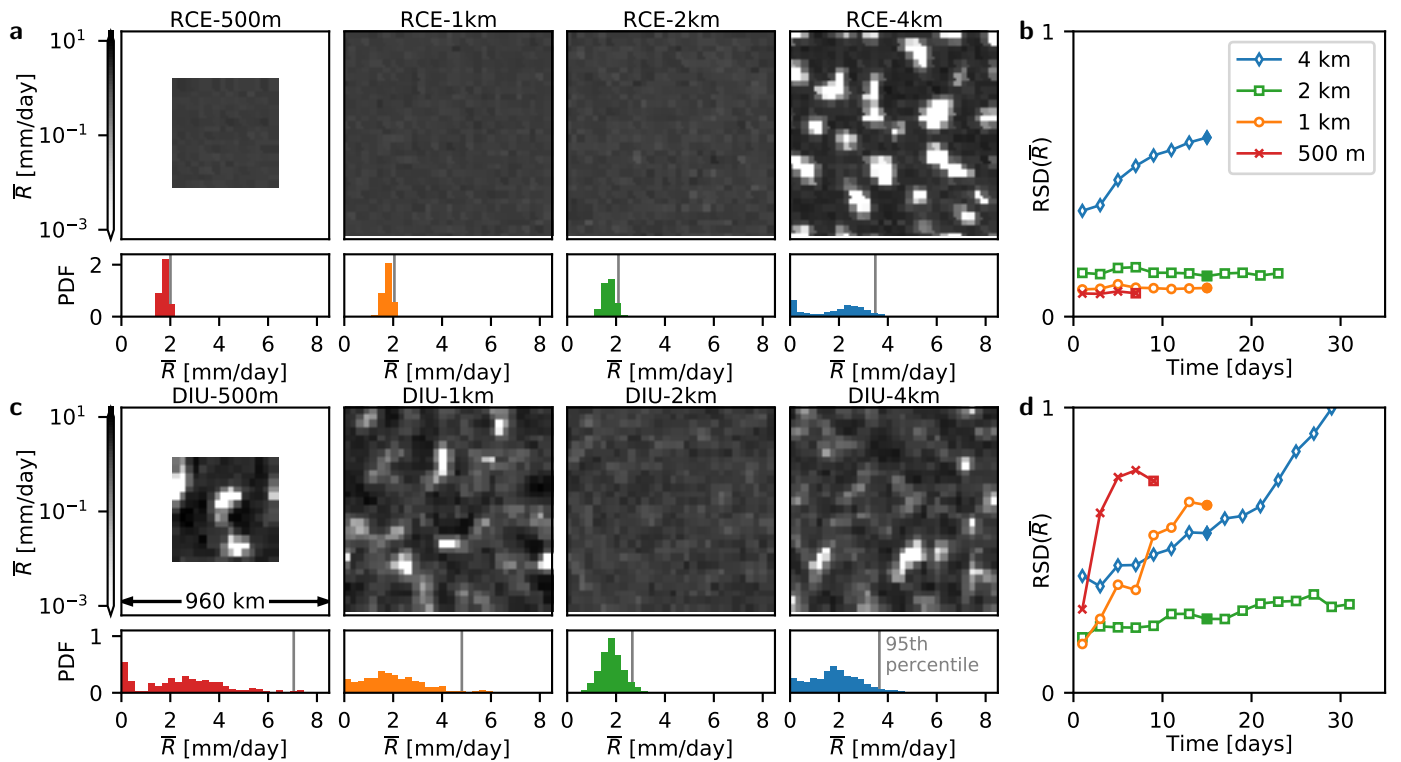


Figure 2: **Aggregation improved at higher resolution.** **a**, Classical CSA under RCE conditions, where the coarse-grained rainfall field  $\bar{R}$  is shown at decreasing resolutions. Note that spatial patterns only emerge at coarse resolution (4 km). The barplots show the histogram of  $\bar{R}$  for the corresponding field in each panel. Grey vertical lines indicate the respective 95th percentile. **b**, Time series of the relative standard deviation of  $\bar{R}$  for each 48-hour period. **c** and **d**, Analogous to (a) and (b), but for DIU. Note that strong phase separation, akin to CSA, now increasingly occurs at finer resolution. Time points used in (a) and (c): RCE-500m:  $t \in [6d, 8d]$ , DIU-500m:  $t \in [8d, 10d]$ , all other cases:  $t \in [14d0h, 16d0h]$ , as indicated by the solid symbols in panels (b) and (d).

considered detrimental to CSA<sup>7,14,16</sup> (Fig. 2c,d). In DIU-2km,  $RSD(\bar{R})$  shows a weaker increase and persistent rain-free patches are all but absent (Fig. 2c,d). These observations lead us to conclude that the diurnal mechanism responsible for producing persistent dry patches is stronger with increasing horizontal resolutions. At very coarse resolution DIU-4km also aggregates at a rate similar to that of RCE-4km. We ascribe this to known CSA feedbacks, acting despite the diurnal cycle.

Extreme precipitation is strongly enhanced for high resolutions in DIU (see grey lines in Fig. 2c). In RCE, extremes remain comparably small at such resolutions. The 99th percentile of daily rainfall—a typical index of extreme precipitation<sup>39</sup>—increases fourfold in DIU compared to RCE at 500m and 1km horizontal resolutions, also measured at horizontal box-size of 32 km $\times$ 32 km (Details: Fig. S2).

## Convective cascades and combined CPs

Why do convective activity aggregate at high resolution for DIU, but not for RCE? We examine the cascade of events leading to different organisational patterns in DIU versus RCE by mapping the low-level horizontal flow using Lagrangian particle tracking. In DIU, seeds are spaced regularly before the onset of precipitation at 1d6h and

passively advected with the horizontal flow during 24 hours (Details: Methods). We perform an analogous particle tracking for RCE. In DIU-500m the final particle positions are visually clustered into stringy structures (Fig. 3a). Such patterns, which we attribute to the gust fronts of combined CPs produced by MCSs, are hardly visible in the coarser-resolution simulation DIU-4km. Also, particles in DIU-500m are generally displaced much further than in DIU-4km, with large cleared spaces opening up in DIU-500m (compare panels in Fig. 3a). To quantify these differences, we compute the distance between the initial and final position of each particle, termed  $\delta$ . The set of distances for all particles yields histograms of  $\delta$  (Fig. 3c) for all simulations. These distributions are all remarkably well-fitted by Rayleigh functions:  $\pi(\delta/2\sigma) \exp[-\pi(\delta/2\sigma)^2]$ . The Rayleigh function describes the radial part of a two-dimensional normal distribution and is consistent with the motion of a random walker. The diffusive length scale  $\sigma$  measures the typical distance travelled. Interestingly,  $\sigma$  systematically increases for DIU as model resolution is made finer. In RCE resolution has no noticeable effect on  $\sigma$ , which is consistently smaller than for DIU (Fig. 3c, grey curves).

For DIU, the continued increase of  $\sigma$  at our highest resolution (DIU-500m) suggests that processes exist, which

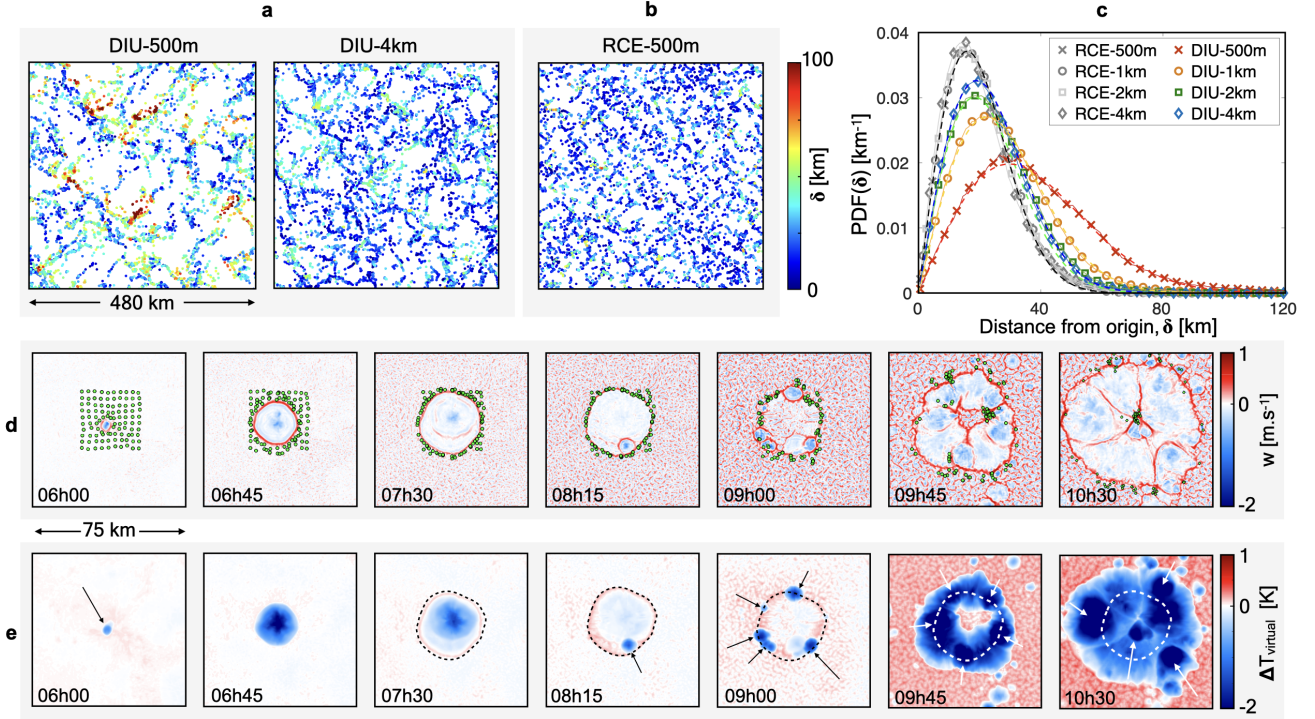


Figure 3: **Low-levels circulation enhanced by resolution and diurnal cycle.** **a**, Final state of the Lagrangian particle tracking analysis in DIU. Particles are seeded along a 4 km square lattice at 1d6h, and plotted at 2d6h and coloured by the respective distance traveled,  $\delta$ . **b**, Analogous to (a) but using RCE-500m. All RCE cases yielded a visually similar particle field and are not presented for conciseness. **c**, Probability distribution functions of  $\delta$ . Dashed lines corresponds to Rayleigh distribution best-fits. The best-fit scale parameters  $\sigma$  are [37.1, 27.2, 24.3, 23.2] km for DIU for  $dx = [0.5, 1.0, 2.0, 4.0]$  km, respectively, whereas  $\sigma = 18.8 \pm 0.9$  km for RCE. **d**, Instantaneous vertical velocity fields at  $z=50$  m during day 1 (exact times as labelled) showing the evolution of a *primo*-CP.  $10 \times 10$  seeds, uniformly-distributed on square lattice with spacing of 4 km, are initialised at 5h to visualise the surface flow. **e**, Analogous to (d) but for the virtual temperature anomaly field  $\Delta T_{\text{virtual}}$  defined as the local difference to the ( $z=50$  m)-horizontal average. Arrows highlight new CPs. The dashed line correspond to the convergence ring of the *primo*-CP front once it has stopped its first expansion phase (*Details*: Methods).

require a mesh even finer than 500 m to become fully activated. What are these small-scale processes which have such a dramatic impact on the low-level circulation? Why are these processes only relevant in DIU, but not in RCE? RCE simulations are characterised by seemingly random eruptions of convective raincells and associated spread of CPs with CP diameters of typically 10 km. These CPs are the main cause of horizontal winds, and they quickly transport tracers from their interior to the gust fronts. However, the disorganised occurrences of new CPs prevent the tracers from travelling long distances effectively.

By contrast, raincells in DIU occur in diurnal bursts, where the first raincells on a given day erupt within a quiescent, but near-unstable, environment (Fig. 3d,e). We term the CP resulting from the initial raincells which succeeds in the competition for the most unstable locus as *primo*-CP. By further destabilising the surrounding environment through positive vertical velocity (Fig. 3d), these *primo*-CPs can set off a cascade of secondary raincell-CP pairs (see 8h15-9h00). The secondary CPs instigate a tertiary population (see 10h30) and so forth. Since such cascades of convective activity can

last for several hours and span more than  $\sim 100$  km we view them as emergent MCSs<sup>28</sup>. This process is driven by the merging of outward-running fronts into an enclosing macrostructure we refer to as *combined CP*<sup>38</sup>. The large areas of the combined CPs result in a more persistent tracer transport (green points in Fig. 3d), explaining the increased mean  $\delta$ 's. Similar MCS-like expansion processes occur throughout the model domain, on the same and on subsequent days. Eventually, the interaction with other combined CPs and diurnally decreasing surface forcing halt further expansion. After the cascade is completed, a large region remains convectively suppressed by the reduced buoyancy of the cold and dry boundary layer (Fig. 3d,e, 10h30). Especially the lack of moisture is responsible for the negatively day-to-day rainfall correlations. Importantly, two conditions have to be met to enable such cascades: (i) strong nocturnal cooling, ensuring quiescent conditions and thus the existence of a *primo*-CP; (ii) a mesh fine enough to resolve the convergence ring and the vertical mass fluxes at its edges — allowing the *primo*-CP to transition into a combined CP. Note that (i) cannot be satisfied by RCE, thus hampering combined CPs.

Conversely, (ii) is likely not met by DIU-2km and DIU-4km, impeding the cascade mechanism and opening for standard CSA feedbacks to take over (see Fig. S3 for additional illustration).

## Genesis of a persistent dry patch

The cascade process described above brings about boundary layer dry anomalies strong enough to suppress convective activity on the following day. But how are dry patches enabled that persist even longer, over many days? Consider the onset of a particular persistent dry patch in DIU-500m (Fig. 4a, red square). The formation of the persistent dry patch is initiated by a strong MCS at  $t \approx 2\text{d}12\text{h}$ . This process leaves the free troposphere relatively moist, but the boundary layer is dried out (Fig. 4d). On the following day, deep convection elsewhere forces pronounced subsidence within the region of interest ( $t \approx 3\text{d}12\text{h}$ ). This subsidence leads to strong drying within the free troposphere, which experiences a change from a moist to a dry anomaly within a single day (Fig. 4d). At this stage the resulting dry anomaly becomes self-sustaining. We attribute that to the well-known moisture-radiation feedback invoked in studies on the maintenance of traditional CSA<sup>3,7,9,16</sup>: the dry free troposphere (Fig. 4a,c) gives rise to increased long-wave cooling (*compare*: Fig. S5i–l), which in turn must be compensated by general subsidence heating (Fig. 4b). Subsidence further amplifies the drying and prevents deep convective activity.

In the boundary layer a circulation is driven by the CP outflow from surrounding deep convective activity (Fig. 4b, 4d18h–24h) and results in significant evening updraughts below  $z \approx 1$  km between days four and eight (Fig. 4c). Such nocturnal low-level updraughts do not initiate new convection because the atmosphere is already stabilised at this time of day.

Outside the dry patches, the dynamics switches from day to day between two modes (Fig. 4a,b blue-boxed and e,f): on some days (eg. 6th, and 8th), mid-day convective activity results in heavy rainfall, increased free-tropospheric moisture, and significant drying in the boundary layer. On other days (eg. 7th and 9th) the dynamics resembles that within the persistent dry patch, with net mid-day subsidence followed by low-level nocturnal updraughts. However, the mid-day subsidence is weaker than in the dry patch, and the free troposphere does not dry below the domain average, so convection is no longer inhibited once the boundary layer has re-moistened. Rapid free-tropospheric drying appears to be a pivotal step in persistent dry patches formation.

Periodic surface temperature forcing can induce persistent dry patches, but can these dry patches prevail when the periodic forcing is removed? To answer this, we extend DIU-500m, starting with its state at 9d18h but replace the DIU with the RCE forcing, that is constant surface temperature and insolation. As might be expected, the DIU-to-RCE switch leads to a gradual relaxation of domain mean atmospheric temperature and rainfall to a near-constant

steady state (Fig. S4). Inspecting total moisture at  $z = 3.5$  km (Fig. 4a and Fig. S5a–h), the spatial partitioning into moist and dry patches is clearly preserved and dry patches sharpening significantly, especially in the boundary layer (Fig. S5d,h). Hence, the transition to RCE causes an alignment of dry patches throughout the vertical column—a feature consistent with classical CSA. The classical CSA trademarks of increased long-wave cooling and the absence of rainfall over dry areas<sup>3</sup> are recovered (Fig. S5i–k, m–o). We conclude that temporary convective organisation under DIU can lead to persistent CSA-like organisation, even after the periodic forcing is removed.

## Implications for tropical climate modelling

The numerical modelling of large-scale thunderstorm clustering was singled out as one of the fundamental questions relevant to the global climate<sup>40</sup>. One prominent explanation for such clustering was CSA,<sup>3</sup> but CSA has been found difficult to achieve at high model resolution when CPs are vigorous<sup>7,9,14</sup>. Our results show that diurnal convective activity spontaneously organises into large-scale spatio-temporal patterns of MCSs and persistently dry patches, especially when model resolution is high, that is, within the limit of greatest practical relevance. Previously, conceptual work attributed the onset of CSA to a linear instability in the free troposphere<sup>8</sup>. In contrast, the onset of persistent dry patches in our simulations is a highly non-linear boundary layer process set off by strongly-correlated CP dynamics. The role of large combined CPs can be seen as inverted, because they can suppress convective activity for long enough to push the troposphere beyond the tipping point at which dry patches become self-perpetuating.

Once formed, dry patches can persist and intensify under temporally constant boundary conditions, with potential consequences for the interface between tropical continents and oceans, such as that between tropical Africa and the Atlantic Ocean: a persistent super-cluster, generated over the continent, could be advected over the sea, where the clustering further intensifies, even under constant surface temperatures. In addition, oceanic surface temperature amplitudes as large as two<sup>41,42</sup> to five kelvin<sup>21</sup> have been observed, and oscillations can persist for up to five days<sup>23</sup>, with a measurable impact on atmospheric properties.<sup>21,23,24</sup>

Regarding extreme convective precipitation, consistently shown to intensify strongly under daily-mean surface temperature increases<sup>39,43,44</sup>, our findings offer a complementary view: extremes can increase, even if the daily-mean temperature is fixed. Our results suggest that convective precipitation extremes are also influenced by the forcing temperature diurnal range and by the state of self-organisation induced by the diurnal cycle.

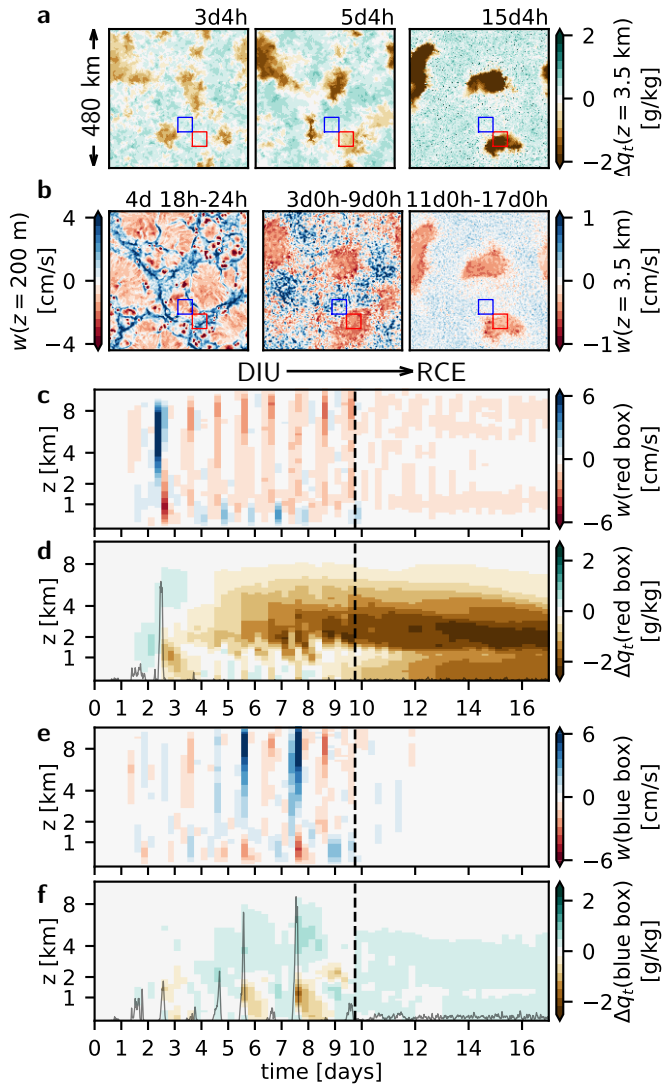


**Figure 4: Onset of a dry patch and transition to RCE.** **a**, Instantaneous nocturnal (4h) horizontal moisture anomaly at  $z = 3.5$  km after 3, 5, and 15 days.  $\Delta q_t \equiv q_t - \langle q_t \rangle$  where  $\langle q_t \rangle$  is the average value at the given temporal and vertical coordinate  $(t, z)$ . **b**, Vertical velocity at  $z = 200$  m (left panel) and  $z = 3.5$  km (centre and right), time-averaged as noted along panels. **c**, Vertical velocity mean, where  $w(t, x, y, z)$  was averaged horizontally within the region marked by red boxes in (a) and (b) and averaged-temporally within six-hour intervals (0h—6h, 6h—12h, 12h—18h, and 18h—24h on each day). **d**, Instantaneous horizontal average of total water mixing ratio,  $q_t(t, z)$ , within the red box at times 4h, 10h, 16h, and 22h on each day. **e** and **f**, Analogous to (c) and (d), but corresponding to the blue box. The dashed lines in panels c–f mark the transition from oscillating (DIU-500m) to constant boundary conditions (DIU2RCE-500m). The grey curves in panels (d) and (f) show time series of average rain intensity in the corresponding regions. In the red box (d) the peak value at  $t \approx 2d12h$  is  $43 \text{ mm h}^{-1}$ .

## Materials and Methods

**Large-eddy model, boundary, and initial conditions.** To simulate the convective atmosphere, we employ the University of California, Los Angeles (UCLA) Large Eddy Simulator (LES) with sub-grid scale turbulence parametrised after Smagorinsky<sup>45</sup>. The Coriolis force and the mean wind are both set to zero. Radiation effects are incorporated using a delta four-stream scheme<sup>46</sup> and a two-moment cloud microphysics scheme<sup>47</sup>. Rain evaporation depends on ambient relative humidity and the mean and spread of hydrometeor radii<sup>48</sup>. Long and shortwave radiation interacts with the atmosphere including clouds, but it does not impact the surface temperature, which is prescribed and spatially homogeneous. The prescribed surface temperature  $T_s(t)$  is spatially homogeneous but oscillates temporally as

$$T_s(t) = \overline{T_s} - T_a \cos(2\pi t/t_0), \quad (1)$$

where  $\overline{T_s} = 298 \text{ K}$ ,  $t_0 = 24 \text{ h}$  is the period of the simulated model day,  $\overline{T_s}$  is the temporal average and  $T_a$  the amplitude of  $T_s(t)$ . For the simulations "DIU"  $T_a = 5 \text{ K}$  is chosen, whereas for "RCE"  $T_a = 0$ . Insolation  $S(t)$  is taken as spatially homogeneous for all simulations. For the simulations "DIU" the insolation cycle  $S(t)$  oscillates temporally with an amplitude typical for the equator. For the "RCE" simulations, both  $T_s(t)$  and  $S(t)$  are set constant to their respective temporal averages, that is,  $T_s(t) = \overline{T_s} = 298 \text{ K}$  and  $S(t) = \overline{S} = 445 \text{ W m}^{-2}$ .

**Surface latent and sensible heat fluxes.** Surface heat fluxes are computed interactively by standard bulk formulae and increase with the vertical temperature and humidity gradients as well as horizontal wind speed. Horizontal surface wind speed is approximated through Monin-Obukhov similarity theory<sup>49</sup>. Our simulations use a simple parametrisation of a homogeneous, flat land surface, by assuming surface latent heat fluxes to be reduced to 70 percent of those obtained for a saturated (sea) surface. For the DIU experiments, mean surface latent and sensible heat fluxes are  $LHF \approx 57 \text{ W/m}^2$  and  $SHF \approx 18 \text{ W/m}^2$ , respectively, yielding a Bowen ratio of  $B \approx .30$ , realistic for forested land. Initial temperature and humidity are taken from observed profiles that potentially represent convective conditions<sup>44</sup>, but quickly self-organise during the initial spin-up. The initial temperature field is perturbed by small uncorrelated noise terms to allow the simulation to break complete spatial symmetry. The spin-up manifests itself in "DIU" by relatively weak precipitation during the first model day, but relatively strong precipitation during the second. From the third day on, precipitation diurnal cycles are found fairly repetitive (*compare*: Fig. 1k). Hence, over time, the system eventually establishes a self-consistent vertical temperature and moisture profile.

**Sensitivity studies.** As we prescribe surface temperature, its value is unaffected by the shortwave diurnal forcing (insolation). Modifications to insolation therefore have only a minor impact on the results: shifting the phase of prescribed surface temperature relative to that of insolation or setting insolation constant, did not yield any qualitative changes

to the diurnal clustering. In addition, taking the surface as a water surface had only minor effects on the diurnal clustering. These and further sensitivities were previously explored in detail<sup>38</sup>. Additionally, we explored changes to initial conditions, by restarting a simulation similar to DIU-1km, but using the horizontal means of temperature and water vapour,  $T(z)$  and  $q_v(z)$ , respectively, obtained after several days of a simulation analogous to RCE-1km, as initial condition. The diurnal clustering and gradual emergence of dry patches was unaffected.

**Model grid, dynamics, and output.** The anelastic equations of motion are integrated on a regular horizontal domain with varying horizontal grid spacing  $dx$  and laterally periodic boundary conditions (Tab. 1). Vertically, the model resolution is stretched, with 100 m below 1 km, 200 m near 6 km, and 400 m in the upper layers. A sponge layer is implemented between 12.3 km and the model top, which is located at 16.5 km. Horizontal resolution  $dx$ , domain size, and output timestep  $\Delta t_{out}$  vary (Tab. 1). At each output timestep, instantaneous surface precipitation intensity, as well as instantaneous horizontal fields of velocity and thermodynamic variables at various vertical levels are recorded. Three-dimensional thermodynamic output data are recorded instantaneously at UTC 4, 10, 16, and 22, whereas three-dimensional velocities are recorded as time averages between UTC 0–6, 6–12, 12–18 and 18–24. Additionally, at 30-second and five-minute intervals, respectively, spatially as well as horizontally averaged time series were extracted from the numerical experiments.

**Temporal correlation.** We define the 24-hour lag correlation  $C_{24h}(q_t; t, z)$  used in Figs 1 and S1 as the pixel-by-pixel Pearson correlation between time  $t$  and  $t + 24h$ , of the horizontal moisture distribution at the vertical level  $z$ :

$$C_{24h}(q_t; t, z) \equiv \sum_{i,j=1}^N \tilde{q}_t(t, x_i, y_j, z) \tilde{q}_t(t + 24h, x_i, y_j, z) \quad (2)$$

where  $N = L/dx$  is the number of grid-boxes along the domain side length (see Tab. 1). The relative spatial anomalies of  $q_t$  at time  $t$  are defined as  $\tilde{q}_t(t, x, y, z) \equiv \Delta q_t(t, x, y, z) / \sigma_{q_t}(t, z)$ , where  $\Delta q_t(t, x, y, z) \equiv q_t(t, x, y, z) - \langle q_t \rangle(t, z)$  is the absolute spatial anomaly of  $q_t$  and  $\langle q_t \rangle(t, z)$  its horizontal average at time  $t$  and vertical level  $z$ ,

$$\langle q_t \rangle(t, z) \equiv \frac{1}{N^2} \sum_{i=1}^N \sum_{j=1}^N q_t(t, x_i, y_j, z)$$

and  $\sigma_{q_t}^2$  is the horizontal variance

$$\sigma_{q_t}^2 \equiv \frac{1}{N^2} \sum_{i=1}^N \sum_{j=1}^N (q_t(t, x_i, y_j, z) - \langle q_t \rangle(t, z))^2.$$

Note that, by definition,  $C_{24h}(q_t; t, z)$  is bounded to lie between  $-1$  and  $+1$ . We compare horizontal fields of  $q_t(t, x, y, z)$  for various values of height  $z$  at  $t$  chosen to represent 4h of each given day. At this time of day the

Experiment name	Surface temperature amplitude, $T_a$ [K]	Horizontal resolution $dx$ [km]	Domain size $L$ [km]	Simulation period [days]	Output timestep $\Delta t_{out}$ [min]
DIU-500m	5	0.5	480	0—10	15
RCE-500m	5	0.5	480	0—8	20
DIU2RCE-500m	0	0.5	480	9.75—17	15
DIU-1km	5	1	960	0—16	20
DIU2RCE-1km	0	1	960	15.75—24	20
RCE-1km	0	1	960	0—16	20
DIU-2km	5	2	960	0—24	20
RCE-2km	0	2	960	0—20	20
DIU-4km	5	4	960	0—42	20
RCE-4km	0	4	960	0—20	20

Table 1: **Summary of numerical experiments.** The term "DIU" is used to indicate simulations with diurnally oscillating surface temperature  $T_s(t)$  and insolation  $S(t)$ , whereas in "RCE" both  $T_s(t)$  and  $S(t)$  are held constant. The term "DIU2RCE" means that "RCE" boundary conditions are applied as a continuation of "DIU" for the respective previous period — such as DIU2RCE-500m, which is initialised with the three-dimensional atmospheric state after 9.75 days. The experiment names further include the respective horizontal model resolution.

atmosphere is generally stably stratified, convective activity is at a minimum and the moisture field is maximally smooth. This is an advantage because we are interested in the large scale structures, and not the precise locations of individual raincells, that typically measure only few kilometres in diameter.

**Coarse-graining procedure.** Coarse-grained rain intensity fields, termed  $\bar{R}$ , are used in Fig. 2 and S2 to compute the relative standard deviation  $RSD(\bar{R})$ , that is, the standard deviation divided by the mean, as well as the exceedence probability of daily precipitation intensity, respectively.  $\bar{R}(k, l, m)$  is a three-dimensional array where each element represent a space-time cube of horizontal interval of length  $s$  and temporal interval of duration  $\tau$ , that is, a cube of volume  $s \times s \times \tau$ . Hence,

$$\bar{R}(k, l, m) \equiv \int_{k\tau}^{(k+1)\tau} dt \int_{ls}^{(l+1)s} dx \int_{ms}^{(m+1)s} dy R(t, x, y),$$

where  $R$  is the model output instantaneous rainfall intensity (Tab. 1). We choose  $s=32$  km spatially. Temporally, Fig. 2 uses  $\tau=48$  h and Fig. S2 uses  $\tau=24$  h. The interval  $s=32$  km is a compromise between being significantly larger than typical individual deep convective rain events yet small compared to the system size. The interval  $\tau=48$  h in Fig. 2 is chosen to emphasise persistent structures and discount the day-to-day anti-correlated, high intensity mesoscale rain clusters. The interval  $\tau=24$  h in Fig. S2 is chosen to capture the natural timescale of one day and make contact to usual extreme event statistics.

**Lagrangian particle tracking.** The particle tracking used in Fig. 3 works in the following way: we distribute a set of seeds over the lowest horizontal level ( $z=50$  m) on the morning of the second day (1d6h). The set forms a squared lattice with one seed placed every 4 km. The particles are then transported over a 24h-period using the horizontal velocity solution and a trapezoidal method with a 15-minute timestep.

We choose to analyse the second simulation day

because: (i) The horizontal morning moisture distribution is increasingly clustered from day to day. Thus earlier days a preferable for disentangling the dynamical effects of cold pools from the thermodynamic preconditioning. (ii) On the first day the rainfall is extremely sparse due to the spin-up from the initial condition. Repeating the analysis on a later days gives comparable results.

In the DIU-experiments we can seed the particles at early morning when there is close to zero convective activity following the nocturnal cooling. This allows us to accurately capture the diurnal motion from onset of convection till the end of the last cold pools. In the RCE-experiments there are no such silent periods, so we have to pick arbitrary beginning and end times for the tracers.

An animation of this process is presented in a supplemental video file.

## **Corresponding Author**

Jan O. Haerter, haerter@nbi.ku.dk

## **Acknowledgements**

The authors gratefully acknowledges funding from the Villum Foundation (grant no. 13168). J. O. H. acknowledges funding from the European Research Council under the European Union's Horizon 2020 Research and Innovation programme (grant no. 771859) and the Novo Nordisk Foundation Interdisciplinary Synergy Program (grant no. NNF19OC0057374). The authors gratefully acknowledge high-performance computing resources from the German Climate Computing Center (DKRZ) as well as the Danish Climate Computing Center (DC3).

## **Author Contributions**

G. G. J. and J. O. H. jointly conceived the project idea and key findings. G. G. J. performed data analysis and produced Figs 1, 2, 4, S1 and S2. J. O. H. performed the numerical simulations, performed data analysis and produced Figs S4 and S5. R. F. performed data analysis and produced Figs 3 and S3. All authors jointly wrote and edited the manuscript.

## **Competing Interest Statement**

The authors declare that they do not have competing interests.

## References

- [1] Held, I. M., Hemler, R. S. & Ramaswamy, V. Radiative-convective equilibrium with explicit two-dimensional moist convection. *Journal of the Atmospheric Sciences* **50**, 3909–3927 (1993).
- [2] Tompkins, A. M. & Craig, G. C. Radiative-convective equilibrium in a three-dimensional cloud-ensemble model. *Quarterly Journal of the Royal Meteorological Society* **124**, 2073–2097 (1998).
- [3] Bretherton, C. S., Blossey, P. N. & Khairoutdinov, M. An energy-balance analysis of deep convective self-aggregation above uniform SST. *Journal of the Atmospheric Sciences* **62**, 4273–4292 (2005).
- [4] Wing, A. A., Emanuel, K., Holloway, C. E. & Muller, C. Convective self-aggregation in numerical simulations: a review. *Surveys in Geophysics* **38**, 1173–1197 (2017).
- [5] Zhang, C. Madden-Julian Oscillation. *Reviews of Geophysics* **43** (2005).
- [6] Emanuel, K. 100 years of progress in tropical cyclone research. *Meteorological Monographs* **59**, 15–1 (2018).
- [7] Muller, C. J. & Held, I. M. Detailed investigation of the self-aggregation of convection in cloud-resolving simulations. *Journal of the Atmospheric Sciences* **69**, 2551–2565 (2012).
- [8] Emanuel, K., Wing, A. A. & Vincent, E. M. Radiative-convective instability. *Journal of Advances in Modeling Earth Systems* **6**, 75–90 (2014).
- [9] Muller, C. & Bony, S. What favors convective aggregation and why? *Geophysical Research Letters* **42**, 5626–5634 (2015).
- [10] Coppin, D. & Bony, S. Physical mechanisms controlling the initiation of convective self-aggregation in a general circulation model. *Journal of Advances in Modeling Earth Systems* **7**, 2060–2078 (2015).
- [11] Hohenegger, C. & Stevens, B. Coupled radiative convective equilibrium simulations with explicit and parameterized convection. *Journal of Advances in Modeling Earth Systems* **8**, 1468–1482 (2016).
- [12] Craig, G. & Mack, J. A coarsening model for self-organization of tropical convection. *Journal of Geophysical Research: Atmospheres* **118**, 8761–8769 (2013).
- [13] Holloway, C. E. & Woolnough, S. J. The sensitivity of convective aggregation to diabatic processes in idealized radiative-convective equilibrium simulations. *Journal of Advances in Modeling Earth Systems* **8**, 166–195 (2016).
- [14] Jeevanjee, N. & Romps, D. M. Convective self-aggregation, cold pools, and domain size. *Geophysical Research Letters* **40**, 994–998 (2013).
- [15] Boye Nissen, S. & Haerter, J. O. Self-aggregation conceptualized by cold pool organization. *arXiv* arXiv:1911.1911 (2019).
- [16] Yanase, T., Nishizawa, S., Miura, H., Takemi, T. & Tomita, H. New critical length for the onset of self-aggregation of moist convection. *Geophysical Research Letters* **47**, e2020GL088763 (2020).
- [17] Moseley, C., Pscheidt, I., Cioni, G. & Heinze, R. Impact of resolution on large-eddy simulation of midlatitude summertime convection. *Atmospheric Chemistry and Physics* **20**, 2891–2910 (2020).
- [18] Hirt, M., Craig, G. C., Schäfer, S. A., Savre, J. & Heinze, R. Cold-pool-driven convective initiation: using causal graph analysis to determine what convection-permitting models are missing. *Quarterly Journal of the Royal Meteorological Society* **146**, 2205–2227 (2020).
- [19] Chen, S. S. & Houze, R. A. Diurnal variation and life-cycle of deep convective systems over the tropical pacific warm pool. *Quarterly Journal of the Royal Meteorological Society* **123**, 357–388 (1997).
- [20] Dai, A. Global precipitation and thunderstorm frequencies. part ii: Diurnal variations. *Journal of Climate* **14**, 1112–1128 (2001).
- [21] Kawai, Y. & Wada, A. Diurnal sea surface temperature variation and its impact on the atmosphere and ocean: A review. *Journal of Oceanography* **63**, 721–744 (2007).
- [22] Suzuki, T. Diurnal cycle of deep convection in super clusters embedded in the Madden-Julian Oscillation. *Journal of Geophysical Research: Atmospheres* **114** (2009).
- [23] Bellenger, H. & Duvel, J.-P. An analysis of tropical ocean diurnal warm layers. *Journal of Climate* **22**, 3629–3646 (2009).
- [24] Bellenger, H., Takayabu, Y., Ushiyama, T. & Yoneyama, K. Role of diurnal warm layers in the diurnal cycle of convection over the tropical indian ocean during miso. *Monthly Weather Review* **138**, 2426–2433 (2010).
- [25] Peatman, S. C., Matthews, A. J. & Stevens, D. P. Propagation of the madden-julian oscillation through the maritime continent and scale interaction with the diurnal cycle of precipitation. *Quarterly Journal of the Royal Meteorological Society* **140**, 814–825 (2014).
- [26] Tan, J., Jakob, C., Rossow, W. B. & Tselioudis, G. Increases in tropical rainfall driven by changes in frequency of organized deep convection. *Nature* **519**, 451–454 (2015).

- [27] Schumacher, R. S. & Rasmussen, K. L. The formation, character and changing nature of mesoscale convective systems. *Nature Reviews Earth & Environment* **1**, 300–314 (2020).
- [28] Houze Jr, R. A. Mesoscale convective systems. *Reviews of Geophysics* **42** (2004).
- [29] Westra, S. *et al.* Future changes to the intensity and frequency of short-duration extreme rainfall. *Reviews of Geophysics* **52**, 522–555 (2014).
- [30] Prein, A. F. *et al.* Simulating North American mesoscale convective systems with a convection-permitting climate model. *Climate Dynamics* 1–16 (2017).
- [31] Fritsch, J. M. & Carbone, R. Improving quantitative precipitation forecasts in the warm season: A uswrp research and development strategy. *Bulletin of the American Meteorological Society* **85**, 955–966 (2004).
- [32] Sukovich, E. M., Ralph, F. M., Barthold, F. E., Reynolds, D. W. & Novak, D. R. Extreme quantitative precipitation forecast performance at the weather prediction center from 2001 to 2011. *Weather and forecasting* **29**, 894–911 (2014).
- [33] Liu, C. & Moncrieff, M. W. A numerical study of the diurnal cycle of tropical oceanic convection. *Journal of the Atmospheric Sciences* **55**, 2329–2344 (1998).
- [34] Tian, B., Waliser, D. E. & Fetzer, E. J. Modulation of the diurnal cycle of tropical deep convective clouds by the MJO. *Geophysical Research Letters* **33** (2006).
- [35] Cronin, T. W., Emanuel, K. A. & Molnar, P. Island precipitation enhancement and the diurnal cycle in radiative-convective equilibrium. *Quarterly Journal of the Royal Meteorological Society* **141**, 1017–1034 (2015).
- [36] Ruppert Jr, J. H. & Hohenegger, C. Diurnal circulation adjustment and organized deep convection. *Journal of Climate* **31**, 4899–4916 (2018).
- [37] Ruppert Jr, J. H. & O’Neill, M. E. Diurnal cloud and circulation changes in simulated tropical cyclones. *Geophysical Research Letters* **46**, 502–511 (2019).
- [38] Haerter, J. O., Meyer, B. & Nissen, S. B. Diurnal self-aggregation. *npj Climate and Atmospheric Science* **3**, 30 (2020).
- [39] Lenderink, G. & Van Meijgaard, E. Increase in hourly precipitation extremes beyond expectations from temperature changes. *Nature Geoscience* **1**, 511–514 (2008).
- [40] Bony, S. *et al.* Clouds, circulation and climate sensitivity. *Nature Geoscience* **8**, 261–268 (2015).
- [41] Weller, R. & Anderson, S. Surface meteorology and air-sea fluxes in the western equatorial pacific warm pool during the toga coupled ocean-atmosphere response experiment. *Journal of Climate* **9**, 1959–1990 (1996).
- [42] Johnson, R. H., Rickenbach, T. M., Rutledge, S. A., Ciesielski, P. E. & Schubert, W. H. Trimodal characteristics of tropical convection. *Journal of Climate* **12**, 2397–2418 (1999).
- [43] Berg, P., Moseley, C. & Haerter, J. O. Strong increase in convective precipitation in response to higher temperatures. *Nature Geoscience* **6**, 181–185 (2013).
- [44] Moseley, C., Hohenegger, C., Berg, P. & Haerter, J. O. Intensification of convective extremes driven by cloud–cloud interaction. *Nature Geoscience* **9**, 748 (2016).
- [45] Smagorinsky, J. General circulation experiments with the primitive equations: I. the basic experiment. *Monthly Weather Review* **91**, 99–164 (1963).
- [46] Pincus, R. & Stevens, B. Monte Carlo spectral integration: A consistent approximation for radiative transfer in large eddy simulations. *Journal of Advances in Modeling Earth Systems* **1** (2009).
- [47] Stevens, B. *et al.* Evaluation of large-eddy simulations via observations of nocturnal marine stratocumulus. *Monthly Weather Review* **133**, 1443–1462 (2005).
- [48] Seifert, A. & Beheng, K. A two-moment cloud microphysics parameterization for mixed-phase clouds. Part 1: Model description. *Meteorology and Atmospheric Physics* **92**, 45–66 (2006).
- [49] Stull, R. B. *An introduction to boundary layer meteorology*, vol. 13 (Springer Science & Business Media, 2012).

# The diurnal path to convective self-aggregation

## — Supplementary Information —

In this supplementary information, we provide further analysis of interest to some expert readers, but not directly relevant for the understanding of the main text.

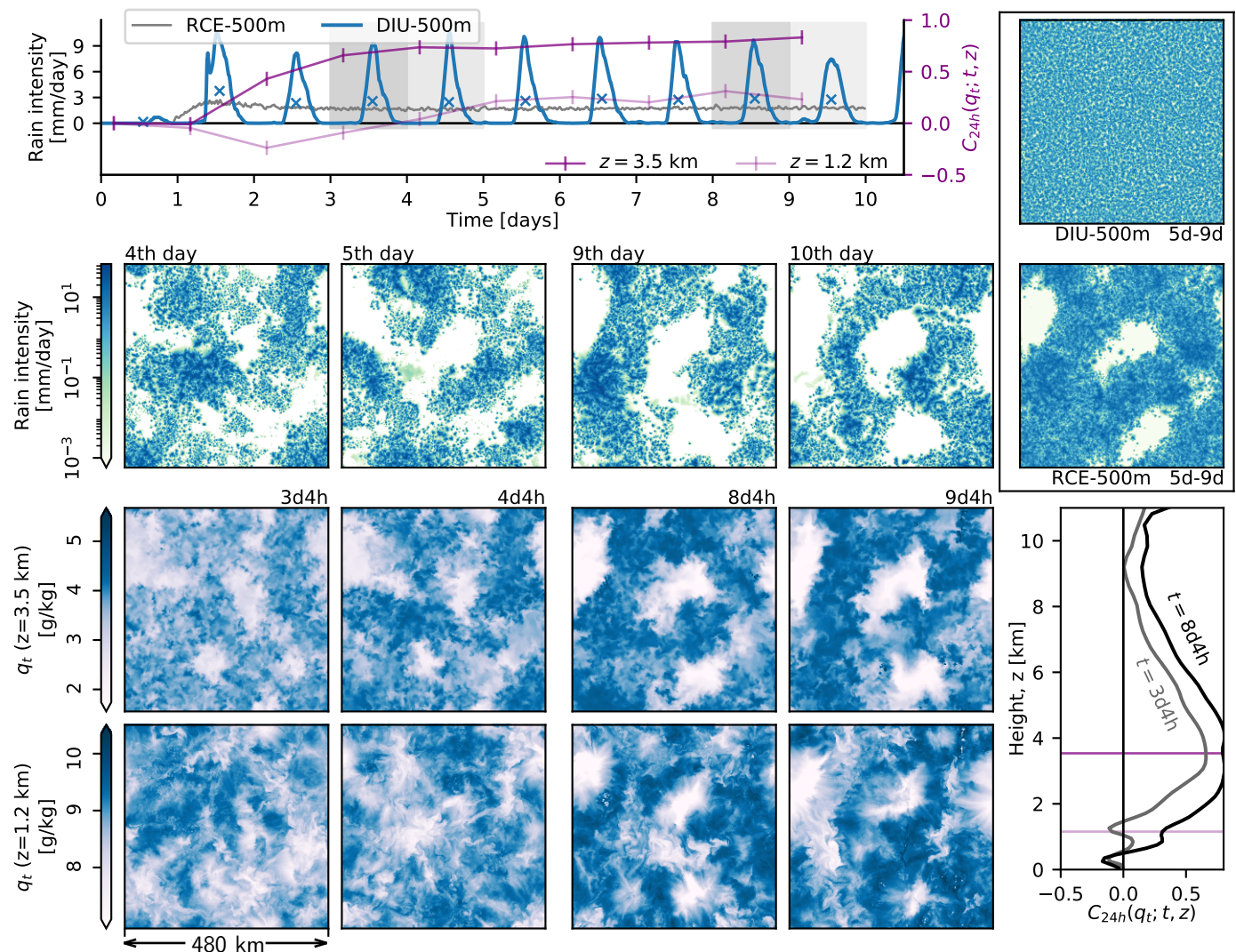


Figure S1: **Spatio-temporal organisation by diurnal surface temperature oscillations (DIU-500m)**. Analogous to Fig. 1, but for DIU-500m and RCE-500m.

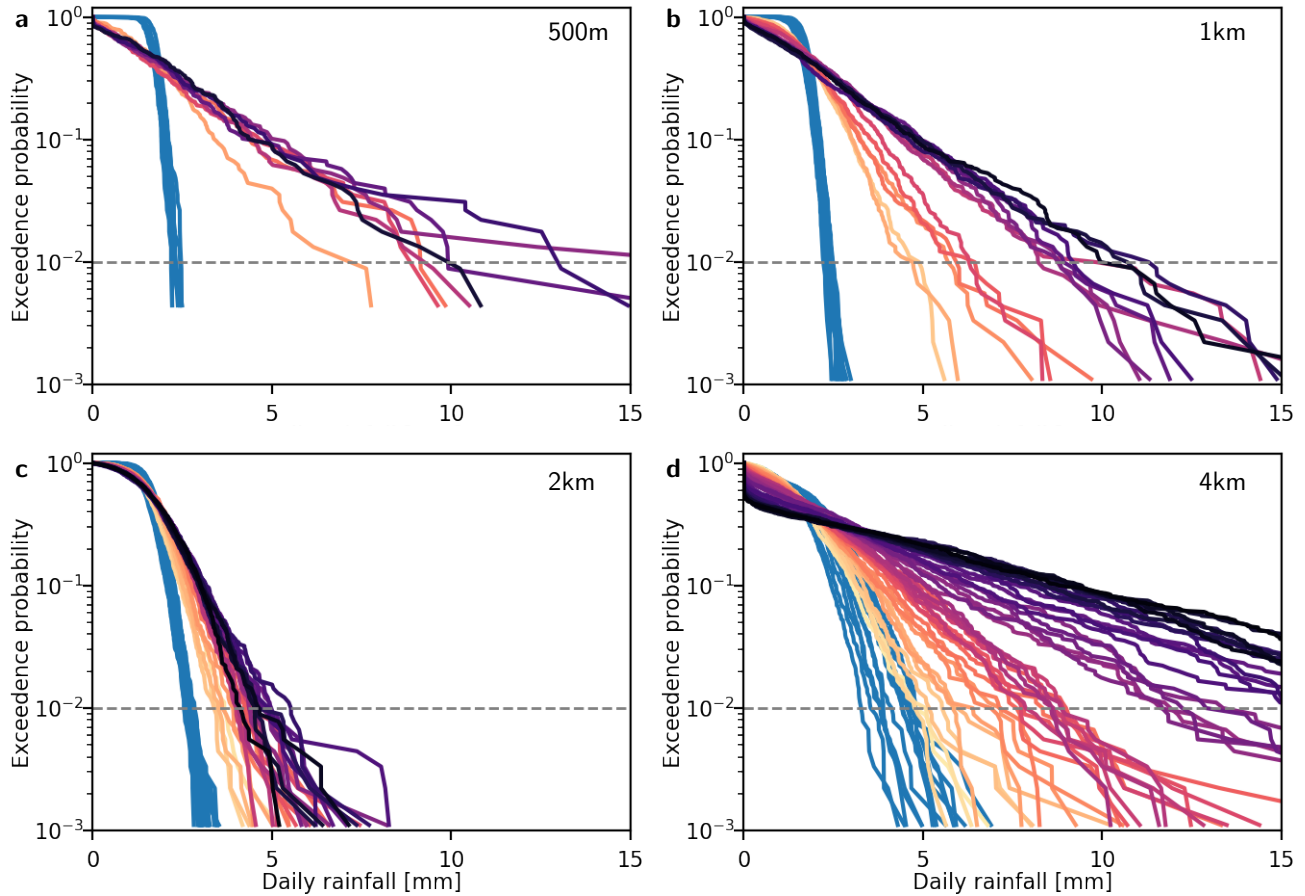


Figure S2: **Daily accumulated precipitation distribution.** The surface rainfall field  $R$  is coarse-grained to boxes of  $32 \text{ km} \times 32 \text{ km} \times 24 \text{ hours}$  (*Details: Methods*), representing daily rainfall averages with squares of  $32 \text{ km}$  side length. For various simulation day, we plot the normalised probability of such daily rainfall averages to lie above any given threshold. Curves of colours in the sequence of yellow-red-purple-black represent distribution functions for consecutive days. Analogously, the blue curves represent the RCE experiments. The first 48 hours are omitted in all datasets, to discard the spin-up period. Panels correspond to horizontal resolutions of: **a**, 500m; **b**, 1 km; **c**, 2 km; **d**, 4 km. In all panels, the grey, dashed horizontal lines mark the 99'th percentiles, as a typical measure of extreme precipitation. Note the pronounced increase in extreme precipitation for the later days of the DIU-simulation, where the 99'th percentile reaches a multiple of that for the RCE-simulation. For all panels, note the logarithmic vertical axis scaling.

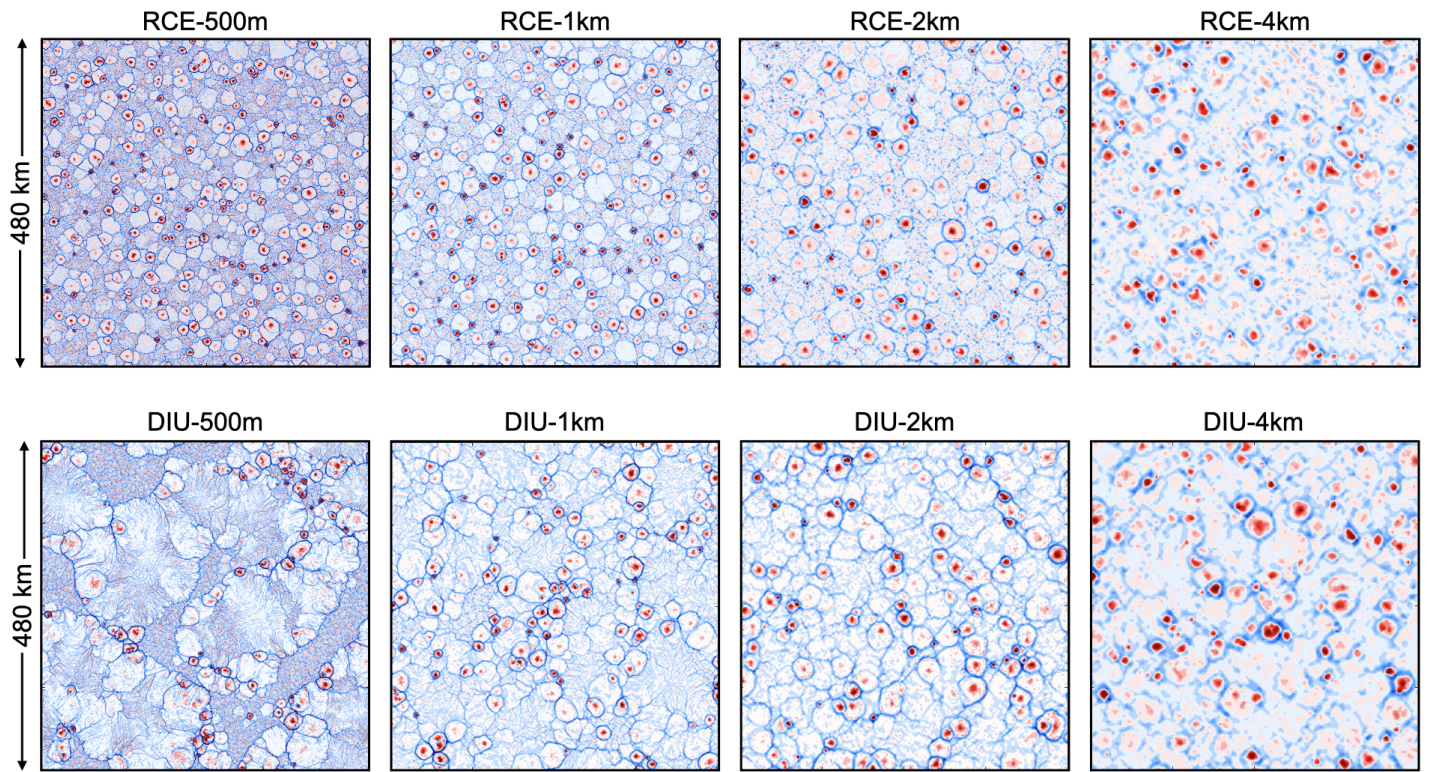


Figure S3: **Contours of surface horizontal velocity divergence fields.** Snapshots of  $\frac{\partial u}{\partial y} + \frac{\partial v}{\partial x}$  are extracted from the first level ( $z=50\text{m}$ ) at 18h00 on the sixth day. The contours range from  $-0.004$  to  $0.004 \text{ s}^{-1}$  (blue to red) and are presented from left to right in decreasing order of spatial resolution for both (top) RCE and (bottom) diurnal configurations.

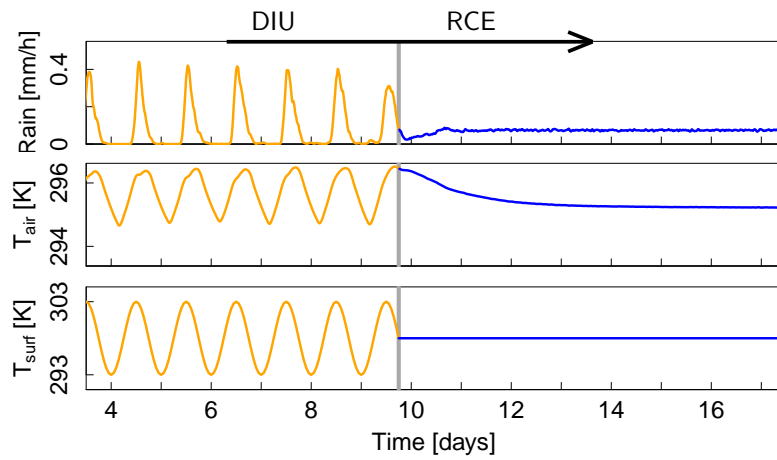


Figure S4: **Domain mean time series for DIU2RCE-500m.** Time series of horizontally-averaged rainfall intensity, near-surface air temperature ( $T(z = 50 \text{ m})$ ) and prescribed surface temperature ( $T_{surf}$ ). Note the transition between temporally-varying (DIU) and temporally constant (RCE) surface temperature at  $t = 9\text{d}18\text{h}$ , as well as the response in  $T_{air}$  and rainfall.

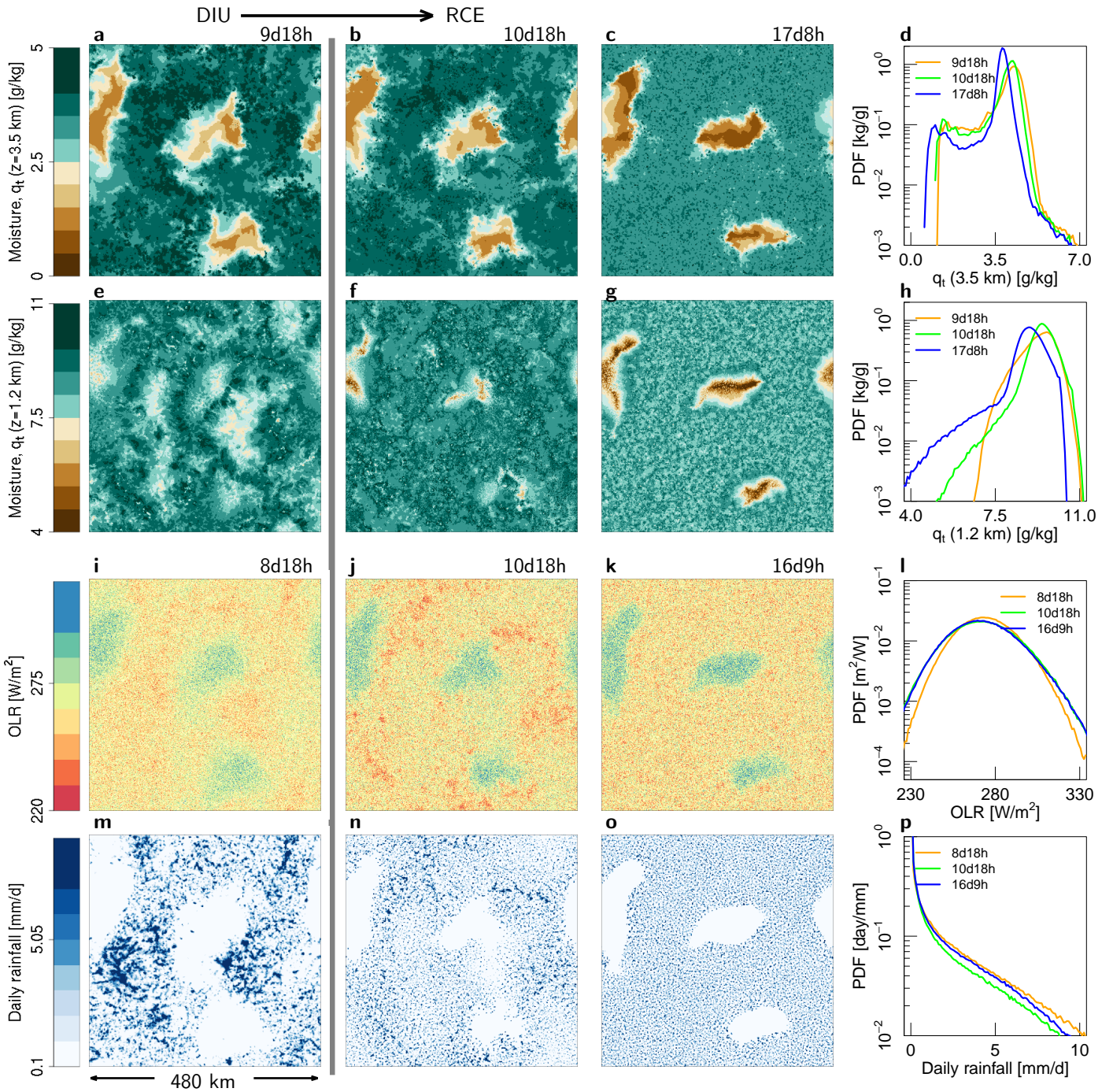


Figure S5: **Transition from DIU to RCE.** **a**, Water vapour mixing ratio anomaly  $q'(z = 3.5 \text{ km}) \equiv q(z = 3.5 \text{ km}) - \overline{q}_t(z = 3.5 \text{ km})$ , where the overline denotes the horizontal mean, at the time of transition between DIU and RCE ( $t = 9.75$  days) for DIU2RCE-500m. **b**, Analogous to (a), but one day after the transition to RCE ( $t = 10.75$  days). **c**, Analogous to (a), but more than six days after the transition ( $t = 17.35$  days). **d**, PDF of  $q_t(z = 3.5 \text{ km})$  for all three times shown in (a)—(c). Note the overall broadening and increasing bimodality of the humidity distribution function with time. **e—h**, analogous to (a)—(d), but for  $q(z = 1.2 \text{ km})$ . **i—k**, Two-day temporal average (centred at the times noted on the panels) of outgoing long-wave radiation (OLR) at the model top. **l**, PDF of OLR, corresponding to the panels (i)—(k). Note the widening of the distribution function. **m—p**, Analogous to (i)—(l) but for rainfall intensity. Note the pronounced spatial structure in the rain field in (m) but the gradual relaxation to a featureless rainy sub-region and a rain-free dry region (n,o). In all histograms the vertical axis is logarithmic.